Biosensors and Bioelectronics 80 (2016) 682–690

Contents lists available at ScienceDirect

Biosensors and Bioelectronics

journal homepage: www.elsevier.com/locate/bios

Multiplexed detection of lectins using integrated glycan-coated microring resonators

Farshid Ghasemi [a], Ehsan Shah Hosseini [a], Xuezheng Song [b], David S. Gottfried [c], Maysamreza Chamanzar [a], Mehrsa Raeiszadeh [d], Richard D. Cummings [b], Ali A. Eftekhar [a], Ali Adibi [a,*]

[a] Department of Electrical and Computer Engineering, Georgia Institute of Technology, Atlanta, GA 30324, USA
[b] School of Chemical and Biomolecular Engineering, Georgia Institute of Technology, Atlanta, GA 30322, USA
[c] Institute for Electronics and Nanotechnology, Georgia Institute of Technology, Atlanta, GA 30324, USA
[d] Department of Biochemistry, Emory University School of Medicine, Atlanta, GA 30324, USA

ARTICLE INFO

Article history:
Received 10 November 2015
Received in revised form
7 January 2016
Accepted 20 January 2016
Available online 27 January 2016

Keywords:
Biosensor
Nanophotonics
Sensor Optimization
Noise
Glycoprotein

ABSTRACT

We present the systematic design, fabrication, and characterization of a multiplexed label-free lab-on-a-chip biosensor using silicon nitride (SiN) microring resonators. Sensor design is addressed through a systematic approach that enables optimizing the sensor according to the specific noise characteristics of the setup. We find that an optimal 6 dB undercoupled resonator consumes 40% less power in our platform to achieve the same limit-of-detection as the conventional designs using critically coupled resonators that have the maximum light–matter interaction. We lay out an optimization framework that enables the generalization of our method for any type of optical resonator and noise characteristics. The device is fabricated using a CMOS-compatible process, and an efficient swabbing lift-off technique is introduced for the deposition of the protective oxide layer. This technique increases the lift-off quality and yield compared to common lift-off methods based on agitation. The complete sensor system, including microfluidic flow cell and surface functionalization with glycan receptors, is tested for the multiplexed detection of Aleuria Aurantia Lectin (AAL) and Sambucus Nigra Lectin (SNA). Further analysis shows that the sensor limit of detection is 2×10^{-6} RIU for bulk refractive index, 1 pg/mm^2 for surface-adsorbed mass, and ~10 pM for the glycan/lectins studied here.

1. Introduction

Integrated photonic resonators are sensitive, on-chip transducers suitable for various sensing applications (Hunt and Armani, 2010; Fan et al., 2008). Their miniature size allows the realization of large microarray sensors on a single chip that is of interest in many biosensing applications such as the detection of DNA (Rong et al., 2008), microRNA (Qavi and Bailey, 2010), toxins (Ghasemi et al., 2013), blood biomarkers (Washburn et al., 2009), and aptamers (Park et al., 2013). The resonance wavelength of a typical resonance-based integrated photonic sensor changes when the desired analyte binds to its surface, resulting in a change in the transmitted power through an optical waveguide that is coupled to the resonator.

Integrated photonic dielectric resonators have been demonstrated in different material platforms including silicon (Si) (Claes et al., 2010), silicon nitride (SiN) (Heideman et al., 2012; Lee et al., 2010), indium phosphide (InP) (Ciminelli et al., 2013), and polymers (Chao et al., 2006). Stoichiometric SiN is an appropriate choice as it is compatible with both CMOS fabrication processes and the majority of surface functionalization protocols. In addition, SiN has a relatively small thermo-optic coefficient (TOC) making the device less susceptible to temperature variations. Despite several temperature compensation techniques proposed for integrated photonic resonators (Gylfason et al., 2010; Kirk et al., 2011), the temperature difference between the sensor and the reference resonators is still a source of device-level thermal noise. Small TOC of SiN results in the suppression of this thermal effect by one order of magnitude compared to Si, InP, gallium arsenide, and titania (Della Corte et al., 2000; Gülsen and Naci Inci, 2002). Furthermore, stoichiometric SiN has two important advantages in terms of the system cost. First, it can be deposited using inexpensive processes such as low-pressure chemical vapor deposition (LPCVD). Second, it is transparent to near infrared and visible wavelengths, which enables the use of low-cost light sources and Si photodetectors in the system.

* Corresponding author.
E-mail address: ali.adibi@gatech.edu (A. Adibi).

http://dx.doi.org/10.1016/j.bios.2016.01.051
0956-5663/

In addition to the material platform, the sensor performance depends on its geometry. A proper figure of merit (FOM) for optimization of a sensor is its limit of detection (LOD) (Chamanzar et al., 2010), defined as the smallest quantity of target analyte that the sensor can reliably detect (Ghasemi et al., 2014). For optimization of LOD in resonance-based sensors, typical design procedures seek to minimize $1/(Q \cdot S)$, where Q is the quality factor of the resonance; and S is its sensitivity, which is defined as the ratio of the resonance shift to the quantity of the analyte bound to the surface of the resonator (Fard et al., 2014). On the other hand, it is a well established design procedure to maximize the signal-to-noise ratio (SNR), with the "signal" typically defined as the extinction of the resonance (i.e., the difference between on-resonance and off-resonance transmitted power). However, in case the optimization requires a compromise between the SNR and Q of the resonator, a unified approach encompassing both of these factors simultaneously is required. Despite important research efforts on the noise performance of resonance-based sensors (White and Fan, 2008), such a unified approach is missing from the literature. Not only this optimization leads to lowest LOD, it is also crucial for large scale integration of highly multiplexed sensors, where power consumption and heat generation are main limitations. In applications where a low LOD is not necessary, the optimization approach described here can be used to minimize the power consumption at the same LOD level.

In this paper, we demonstrate a new concept for the optimization of power consumption in resonance-based integrated photonic sensors. We argue that to achieve optimal LOD, the resonance lineshape curvature at the resonance wavelength is the single important parameter of the lineshape that should be optimized. This parameter includes the contributions of both the linewidth and the extinction (or equivalently, Q and SNR), and thus shrinks the design space into only one dimension. The waveguide-resonator spacing is then used to tune the coupling strength, which in turn tunes the resonance curvature (i.e., the curvature of transmitted power curve of the bus waveguide in the wavelength domain at the resonance wavelength). On the experimental side, a full biosensor based on the optimized elements is fabricated and functionalized with glycan bioreceptor molecules. Glycans are carbohydrate molecules that specifically recognize toxins and other bio-functional molecules (Smith et al., 2010; Song et al., 2011). The solution of target molecules is delivered through a microfluidic flow cell to reduce the response time and minimize the required sample volume (De Vos et al., 2007). Our results show that our optimized sensor can detect multiple analytes with LOD of 1 pg/mm^2 for surface-adsorbed mass, which corresponds to a bulk refractive index LOD of 2×10^{-6} RIU (Refractive Index Unit).

In Section 2, we explain device concept, fabrication, and sensor packaging. The optimization of the resonator-waveguide coupling of the sensor is elaborated in Section 3. The sensor is used for label-free, specific, and multiplexed detection of Aleuria Aurantia Lectin and Sambucus Nigra Lectin as described in Section 4. The discussion and conclusions are presented in Sections 5 and 6, respectively.

2. Materials and methods

2.1. Sensor device nanofabrication

The sensor array consists of five SiN microring resonators coupled to a common bus waveguide, as shown in Fig. 1a. The width of the bus waveguide and the microrings is 500 nm to ensure single-mode operation. The outer radius of each microring is about 8 μm. Slight offsets in the radii of the microrings result in the spectral offsets of their resonance wavelengths. This offset prevents resonance overlap in the spectral domain to avoid crosstalk problem for multiplexed sensing. It should be noted that the addition of organic bio-receptor layers also shifts the resonances of these microring resonators, depending on the size of the bio-receptor molecule and its surface density. This fact should be taken into account if the resonances are to be designed equidistant in the spectrum.

The device thin film stack is fabricated by thermal oxidation of a standard eight-inch Si wafer to grow 4 μm thermal silicon dioxide (SiO_2) followed by the deposition of 240 nm stoichiometric SiN using LPCVD. Thermal oxidation and SiN deposition are performed by Rogue Valley Microsystems (Medford, OR, USA). The device pattern is written into ZEP520A electron-beam resist (Zeon Corp.) by a JEOL JBX-9300FS electron-beam lithography (EBL) system, and transferred into the SiN layer by inductively coupled plasma etching using CF_4 chemistry, leaving no SiN pedestal. Standard ZEP520A spin-coat protocol and a dosage of 220 μC/cm^2 is used for the EBL. We spin ESPACER 300Z (Showa Denko K.K.; Singapore) on baked ZEP520A to prevent excessive EBL charge-up. The resist is rinsed by de-ionized (DI) water for 1 min, developed for 2 min in amyl acetate, and then soaked for 30 s in isopropyl alcohol (IPA). The residual resist after etching is stripped using Microposit remover 1165 (Shipley).

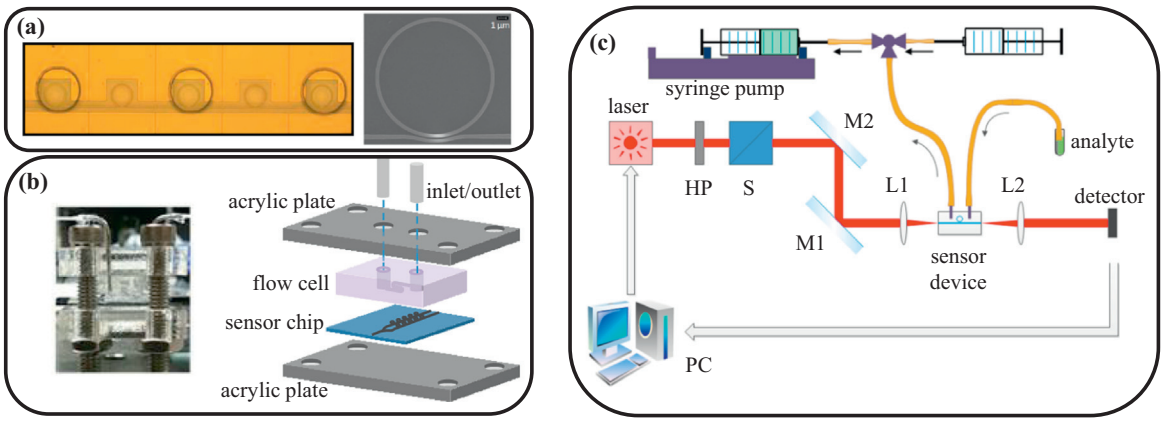

Fig. 1. The components of the sensing system. (a) An optical micrograph of the array of five SiN microrings (left), and a scanning electron micrograph of a SiN microring (right). The width of each microring is 500 nm to ensure single-mode operation, and its outer radius is about 8 μm. (b) The sensor chip, PDMS flow cell, and holder structure assembled together. (c) Laser light goes through a half-wave plate (HP), a polarizing beam splitter (S), two alignment mirrors (M1 and M2), and a long-working-distance lens (L1). Using a second long-working-distance lens (L2), the light leaving the chip is projected onto a photodetector, the data of which is sampled by a data acquisition card and processed by a personal computer (PC). A syringe pump in negative pressure mode draws the analyte solution into the PDMS flow cell and then into a waste syringe.

2.2. Protective layer: oxide lift-off

Oxide deposition and lift-off are performed to open circular windows above the three sensing microrings on an otherwise oxide-covered chip. To do so, Shipley 1827 resist is spin coated at 500 RPM for 10 s and then 4000 RPM for 60 s, followed by 1 min bake at 150 °C on a hotplate. Photolithography is done using 365 nm UV light with a dosage of 150 mJ/cm^2. Subsequently, the chips are developed in Microposit MF-319 for 50 s with gentle agitation, and then rinsed in DI water. A final one-minute descum in oxygen plasma removes the residual resist to promote the adhesion between the SiN film and the oxide layer. As a result, the three sensing microrings are covered by the Shipley 1827 resist while the rest of the substrate is exposed. Using low-temperature plasma-enhanced chemical vapor deposition (PECVD), 2 µm of protective oxide is deposited on the chip at a temperature of 100 °C. Next, the chip is submerged in acetone for 10 min and then gently brushed with an acetone-soaked swab to remove the residue of Shipley 1827 resist and expose the sensing microrings. The chip is finally cleaved to make the waveguides accessible at the edges of the chip for input/output laser coupling. We found the use of a swab more reliable than an ultrasonic bath for oxide lift-off. The force applied by the swab is mainly exerted to the bumps created by the circular patterns of the resist, as opposed to other flat areas. Since the adhesion of low-temperature oxide to the SiN layer is not strong, the ultrasonic agitation can lift the oxide off at undesired areas.

2.3. Surface chemistry

The SiN surface adsorbs biomolecules through various non-specific mechanisms. These mechanisms make the sensor respond to the presence of undesired molecules. To increase the sensor specificity, we covalently immobilize bio-receptor molecules on the surface of the sensor. In the first step, the –OH bonds of the surface of the chip are activated by cleaning it with piranha (5:1 mix of H_2SO_4 and H_2O_2) for 30 min, a DI water rinse, and a 10 min exposure to UV/ozone plasma in a UVOCS® cleaner. The chips are then immersed in a 2% v/v solution of (3-mercaptopropyl)trimethoxysilane in anhydrous toluene for one hour (in a nitrogen ambient), thoroughly rinsed with IPA, dried, and baked at 80 °C for 20 min. When the samples cool down, a drop of 2 mM SM(PEG)12 linker (Pierce; Chicago, IL, USA) in anhydrous dimethyl sulfoxide (DMSO, from Acros Organics; Pittsburgh, PA, USA) is placed on the chip to cover its surface. The sample is left unperturbed in a nitrogen ambient for about 12 h, and then thoroughly rinsed with IPA. SM(PEG)12 linker contains a polyethylene glycol (PEG) chain that helps reduce the non-specific binding of undesired molecules to the surface (De Vos et al., 2009). At this stage, carboxyl functional groups containing N-Hydroxysuccinimide (NHS) esters are covalently grafted on the surface and can immobilize any molecules containing amine functional groups. Fig. 2a shows a schematic representation of the NHS activation protocol. All chemicals, except SM(PEG)12 and DMSO, were obtained from Sigma-Aldrich (St. Louis, MO, USA).

A 200 mM solution of amine-derivatized glycan (Song et al., 2009) is printed selectively on the microrings using a BioForce Nano eNabler. Using this tool, each microring can be coated with a specific glycan. Prior to the printing, the specific glycan solution is mixed 1:1 with phosphate buffered saline (PBS, pH 7.4) containing 10% glycerol to impede evaporation of the glycan solution in the open-top reservoir of the printing cantilever. After the glycans are printed, the chip is left at a relative humidity of 80% to prevent evaporation of the printed droplets. This allows the glycan molecules to bind to the surface through their amine functional groups.

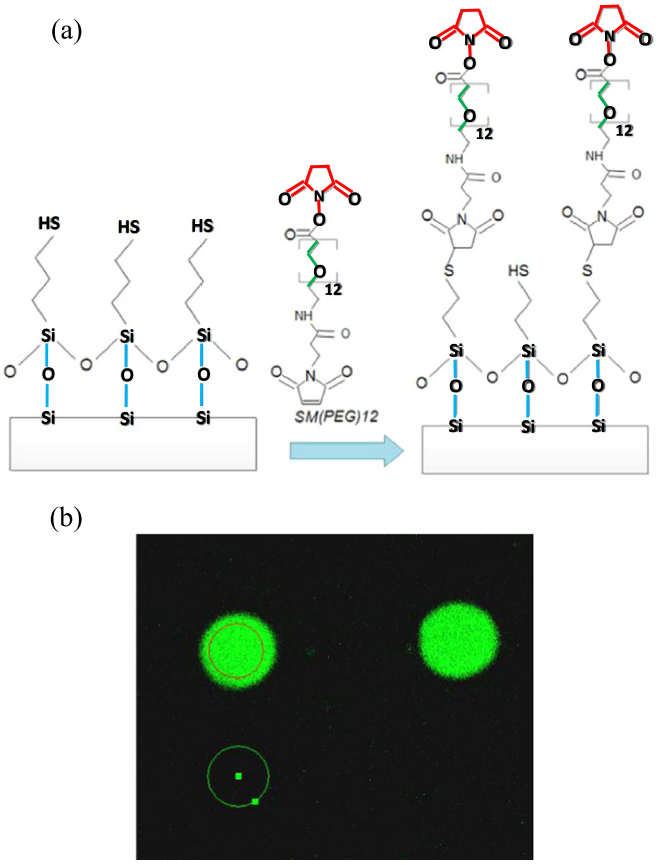

Fig. 2. (a) Schematic representation of the surface chemistry for NHS activation on the SiN surface. Blue (Si-O-Si): siloxane functional group; red ($C_4H_5NO_3$): NHS ester; green ($(O\text{-}CH_2\text{-}CH_2)_{12}$): PEG. (b) A fluorescence microscope image showing selective binding of CTB to GM1 glycan with negligible binding to the areas lacking GM1 (but having a PEG brush). The average fluorescence signal intensity is about two orders of magnitude larger in the areas containing GM1 receptors than otherwise. (For interpretation of the references to color in this figure caption, the reader is referred to the web version of this paper.)

Next, the sample is incubated in a high humidity (at about saturation) chamber at 50 °C for 1 h. The chips are dried and thoroughly washed in a PBS solution with 0.05% Tween 20, and then in DI water. Remaining NHS esters are de-activated in a solution of 50 mM ethanolamine in 0.1 M Tris buffer (pH 9.0) for 1 h. This finalizes the glycan immobilization step and prepares the chip for microfluidic integration.

To verify the efficacy and specificity of the activated surface, we tested the binding of the glycans using fluorescence microscopy. GM1 glycan (von Gunten et al., 2009) was immobilized using the above-mentioned protocol on the SiN surface, and a 50 µg/ml drop of biotin conjugated Cholera toxin B subunit (CTB from Sigma Aldrich; St. Louis, MO, USA) was placed on the surface for 1 h. The SiN surface was then thoroughly washed with PBS solution containing 0.05% Tween 20, and then by DI water. Subsequently, a 200 µg/ml drop of Alexa 488 conjugated Streptavidin (Life Technologies; Carlsbad, CA, USA) was placed on the surface for 1 h, followed by same wash process mentioned above. Fig. 2b shows an image of the surface using a Carl-Zeiss LSM 710 confocal fluorescence microscope. The bright spots in this figure correspond to the areas where the glycans have been printed. In these areas, the glycans capture biotin-CTB, and then biotin-CTB captures Alexa-Streptavidin. In other areas, biotin-CTB and thus, Alexa-Streptavidin cannot effectively bind to the PEG-coated surface. The image shows a high contrast between the glycan-coated areas and the rest of the surface, which demonstrates a low non-specific binding on the areas lacking glycan receptors.

2.4. Microfluidic integration

After glycan immobilization, a polydimethylsiloxane (PDMS) microfluidic flow cell is aligned to the SiN sensor chip using Finetech flip-chip bonder. The microfluidic flow cell helps reduce the response time of the sensor by overcoming the diffusion barrier. As illustrated in Fig. 1b, two acrylic plates hold the chip and the flow cell together by applying a gentle force exerted by four cap screws and nuts at the corners. The acrylic plates are cut using a Hermes lasercutter machine. After assembling the structure, inlet and outlet needles are inserted into the holes made by a puncher in the PDMS flow cell. A syringe pump in negative pressure mode draws the analyte, with a flow rate of 2 μL/min into the input tube, the microfluidic chip, and finally the output tube. The microfluidic channel is 100 μm wide and 50 μm high, and it is cast using an SU-8 mold.

To make the mold, SU-8 2050 (MicroChem; Newton, MA, USA) is spin coated on a Si wafer (500 RPM for 10 s, then 2000 RPM for 60 s), and baked at 95 °C for 5 min. The pattern of the microfluidic channel is written into the resist using a Microtech LW405 laserwriter. The sample is then baked, first at 65 °C for 1 min, and then at 95 °C for 4 min. Unexposed resist is removed by 6 min development in SU-8 developer (MicroChem; Newton, MA, USA). The sample is rinsed and cleaned with acetone and IPA, and further baked at 250 °C for 30 min. This finalizes the preparation of the mold.

To cast PDMS, Dow Corning Sylgard 184 PDMS base and curing agent (Ellsworth; Loganville, GA, USA) are mixed 10:1 (w/w), stirred well, and degassed in vacuum for about one hour. The mixture is poured into the mold, degassed in vacuum for about one hour, and baked at 90 °C for about 10 h to produce the PDMS microfluidic flow cell.

2.5. Biosensor characterization setup

As shown in Fig. 1c, light from a tunable laser (652–660 nm, Newport TLB 6305) is passed through a half-wave plate, a polarizing beam splitter, and a long-working-distance lens to have it focused at the input facet of the sensor chip. Dominant polarization axis of the laser light is rotated by the half-wave plate (HP) to make its magnetic field parallel to the surface of the sensor chip (TM polarization). The light exiting the output waveguide is projected onto a photodetector (Thorlabs PDA36A silicon amplified detector) using another long working distance lens. The laser is controlled by LabVIEW software that scans the wavelength over the 652.4–660 nm window, while the readout of the photodecetor is synchronously recorded by a USB-6211 National Instrument data acquisition (DAQ) device. The readout is de-noised in LabView software using a third order Butterworth low-pass filter with a cut-off frequency of 100 Hz. The laser scan rate is 1 nm/s, and sampling resolution is 0.25 pm. Normalized transmission spectrum is calculated by dividing the transmitted power to the baseline power. The baseline power is calculated by low-pass filtering the transmitted power to remove higher frequency features of the spectrum. An in-house data analysis software in MATLAB environment tracks the resonance shifts in time.

3. Theory: optimization

3.1. Figure of merit

Waveguide-resonator coupling, as seen in Fig. 1a, determines the extinction and the loaded Q of the resonance. The strength of this coupling depends on the gap between the waveguide and the resonator. Proper choice of this gap helps maximize resonance sharpness. A sharper lineshape helps detect the resonance more accurately at any specific noise level (Ghasemi et al., 2015).

An important aspect of the resonance detection procedure is the data processing algorithm employed to extract the resonance wavelength from the experimental data. In this paper, we use a quadratic fit to the data around the resonance as the resonance detection algorithm. A quadratic fit using linear regression is a fast, universal, and versatile method that can rival more sophisticated but sensitive detection methods such as a nonlinear parametric fit (Gylfason et al., 2010). Although parametric fits in general are more accurate when we have an accurate parametric model of the lineshape (e.g., Lorentzian function), in practice the uncertainty about the actual resonance function limits the performance of these parametric fits. The discrepancy between the model and actual lineshape comes from various sources of reflection in the device, such as fabrication imperfections, and the edges of circular openings on the waveguides, which result in lineshape deformation. In this condition, a Lorentzian fit does not necessarily lead to more accurate detection of the resonance wavelength. In contrast, for the majority of mechanisms leading to a lineshape deformation, the lineshape generally follows a quadratic function around the resonance wavelength.

The Lorentzian lineshape of a microring resonance can be approximated by a quadratic polynomial around the center of the resonance lineshape. The quadratic polynomial is determined by two parameters: its curvature (κ_0) and the amplitude of its minimum point (i.e., a vertical offset). The latter does not affect the resonance detection accuracy because a homogeneous shift in the amplitudes of all data points does not shift the resonance along the wavelength axis. Thus, as far as detection accuracy is concerned, the only important parameter is the lineshape curvature.

Besides the lineshape curvature, noise level should also be considered in the coupling optimization. If the noise is intensity-independent, the extinction of the resonance does not affect the noise level. However, for an intensity-dependent noise, the extinction determines the noise level around the resonance dip. It is therefore necessary for the optimization procedure to simultaneously minimize the noise level (σ_n) while maximizing the curvature (κ_0). The end goal of this optimization is to minimize the error in resonance detection when the measurement contains noise. In this regard, it should be noted that an identical scaling of all measurements (i.e., the lineshape and the noise level) does not change the resonance detection accuracy. Hence, we would like the FOM not to change under such a scaling. Hence, we define the FOM as the ratio of σ_n and κ_0, since both parameters scale identically and the scaling factor is eliminated from their ratio:

$$\mathrm{FOM} = \frac{\sigma_n}{\kappa_0}. \tag{1}$$

Although we introduced the FOM in Eq. (1) through a discussion of its desired requirements, a rigorous analysis of our resonance detection method (using a quadratic fit) supports this definition for FOM (Ghasemi et al., 2015). By using the FOM defined in Eq. (1), the SNR need not be optimized separately from Q. This FOM is the ultimate criteria for optimizing the performance of the sensor in terms of the amplitude noise, which is the objective of the optimization of Q and SNR.

3.2. Noise measurement for calculation of FOM

To calculate the FOM in Eq. (1), we first study σ_n in the numerator. To measure the intensity dependence of noise in our setup, we replace the sensor chip with a polarizer. The polarizer acts as a variable attenuator since the laser light has a major axis of polarization. At any specific wavelength, the sensor device is a linear system with a determined attenuation (and a phase

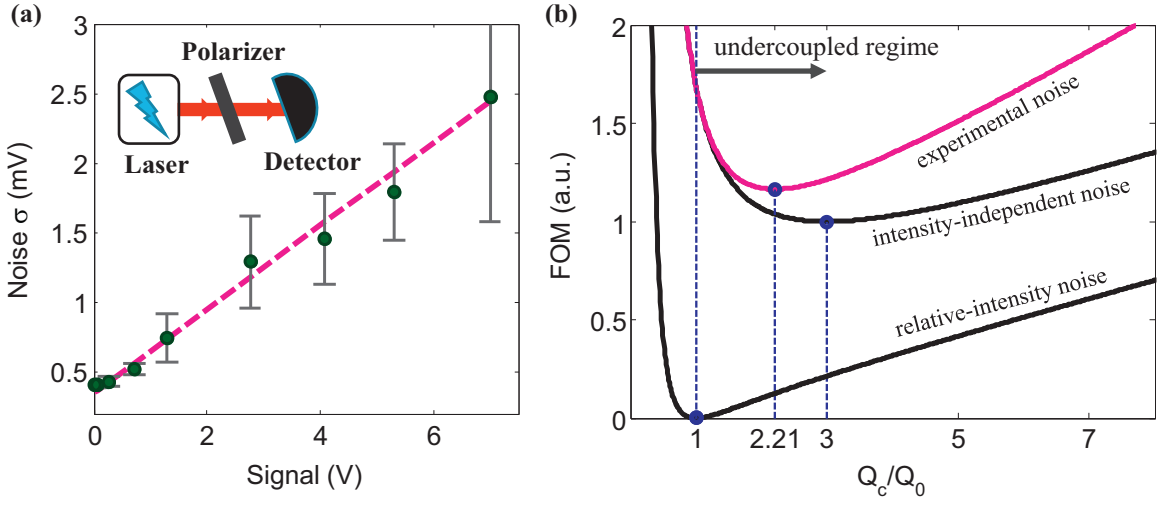

Fig. 3. (a) Measured noise intensity as the average intensity of incoming light on the photodetector changes. Since the laser output is partially polarized, a polarizer serves as a variable attenuator to control the average intensity of the light on the photodetector. (b) The FOM (Eq. (5)) for different ratios of coupling Q (Q_c) and the intrinsic Q (Q_0). The FOM corresponding to the experimentally measured noise is compared with the theoretical cases for intensity-independent noise ($\sigma_n = 0.35$ mV) and relative-intensity noise ($\sigma_n = 0.3\,V$(mV)). The circles show the optimal FOM on each curve.

response that is not picked up by the photodetector). Thus, an attenuator can be used to measure the effective noise on every data point of the spectrum.

For noise measurement, the laser wavelength is scanned from 652.4 nm to 660 nm with a constant current of 43.5 mA. Photodetector gain is set to 40 dB. Since laser output power varies slowly over the scan window, the baseline is calculated by applying a 21-point moving average filter to the data in MATLAB environment. The difference between the raw readout and the baseline is considered as the noise. For each specific attenuation (i.e., polarizer angle), the standard deviation of noise (σ_n) is calculated over the data in the 654–659 nm window. The resulting curve in Fig. 3a shows the intensity-dependence of noise as

$$\sigma_n = 0.35 + 0.3V \ \text{(mV)}, \tag{2}$$

where V is the average light intensity on the photodetector, expressed in terms of the equivalent voltage that the photodetector generates at its output (including the amplification, in Volts). Since we detect resonance dips here, only the noise level for near-zero signals ($V \sim 0$) matters in this optimization.

On the other hand, the resonance curvature (κ_0) and its extinction can be calculated using coupled-mode theory (CMT) (Soltani et al., 2010). The power transmission through a device with a single microring, $T(\lambda)$, is (Shah Hosseini et al., 2010)

$$T(\lambda) = \frac{P_{out}}{P_{in}} = \left| \frac{-2j(\lambda - \lambda_0)/\lambda_0 + 1/Q_0 - 1/Q_c}{-2j(\lambda - \lambda_0)/\lambda_0 + 1/Q_0 + 1/Q_c} \right|^2. \tag{3}$$

Here, λ_0 and Q_0 are the resonance wavelength and the intrinsic Q of the microring, respectively. The observation wavelength is denoted by λ, and the coupling quality factor by Q_c. The curvature of this lineshape at its resonance is

$$\kappa_0 = V_0 \frac{\partial^2 T}{\partial \lambda^2}\bigg|_{\lambda=\lambda_0} = 32 V_0 \left(\frac{Q_0}{\lambda_0}\right)^2 \frac{(Q_c/Q_0)^3}{(1 + Q_c/Q_0)^4}, \tag{4}$$

in which V_0 denotes the photodetector voltage readout for an all-pass transmission.

The FOM can be calculated using the noise characteristics from Eqs. (2) and (3) and resonance curvature from Eq. (4). Assuming a typical all-pass voltage of $V_0 = 1$ V through the device and arbitrary but constant λ_0 and Q_0, our optimization goal is to minimize Eq. (1):

$$\text{FOM} = \frac{\sigma_n(V_0 T(\lambda_0))}{\kappa_0}. \tag{5}$$

We use experimental noise measurements along with Eq. (4) for κ_0 to calculate the FOM. The result is plotted in Fig. 3b for different values of Q_c/Q_0. Optimum coupling occurs for $Q_c/Q_0 \approx 2.21$, which corresponds to an extinction of about 8.5 dB (undercoupled).

3.3. Optimal coupling condition

It is a widely invoked optimization rationale to choose sensor parameters so that the light–matter interaction is maximized. This condition is achieved at the critical coupling regime, where $Q_c/Q_0 = 1$ (Chao et al., 2006). However, as it is seen in Fig. 3b, the FOM at its optimal point is about 0.69 times that at the critical coupling regime. This means, the LOD improves by 31% if the optimal coupling, where $Q_c/Q_0 = 2.21$, is used rather than critical coupling. The reason is that using a quadratic fit for resonance detection, the $3\sigma_\lambda$ error in resonance detection linearly depends on the FOM defined here; and LOD, in turn, depends linearly on the $3\sigma_\lambda$ error (Ghasemi et al., 2015). In inferring this conclusion for the LOD improvement, it is assumed that the designs are compared for a similar input power.

Alternatively, the improvement in the FOM is equivalent to power consumption reduction at a fixed LOD. An example of a condition at which the optical power is adjusted to meet a determined LOD is when the device performance is limited by noises other than additive amplitude noise (e.g., biochemical noise or wavelength noise). In this case, it is desired to set the power so that the contribution of the amplitude noise to the total $3\sigma_\lambda$ is about the same as that from the other dominant sources of noise (Ghasemi et al., 2014). Any further increase of the power will be mostly wasted as the device is already limited by the other noise mechanisms. In this sense, a critically coupled resonator will require 31% more power to achieve the same performance as the optimized device discussed above.

4. Results

4.1. Saltwater titration

We performed an initial round of fabrication with varying

waveguide-resonator gaps to find the gap resulting in an under-coupled 8.5 dB extinction. Next, we conducted saltwater titration to measure the bulk sensitivity of the resonators. Bulk sensitivity is defined as the resonance shift normalized to the refractive index change in the cladding material. The sensor was tested with different concentrations of saltwater and the resonance shifts were measured eight times for each concentration (data not shown here). Having the refractive index of saltwater (Quan and Fry, 1995) for different concentrations at 25 °C, the experimental bulk sensitivity is calculated to be 49 nm/RIU (RIU is the refractive index unit of the clad). The numerical simulation of the microrings in the COMSOL environment results in a bulk sensitivity of 48.1 nm/RIU. In this calculation, refractive indices of SiN, SiO_2, and water clad were assumed to be 2.05, 1.44, and 1.33, respectively.

4.2. Lectin detection: individual tests

We immobilized amine-derivatized (Song et al., 2009) 3-fucosyl lactose (3FL) on two of the exposed microrings for specific detection of biotinylated Aleuria Aurantia Lectin (AAL). All the glycans and lectins in this work were purchased from Vector Labs (Burlingame, CA, USA). The glycan solution was not printed on the middle microring so that this microring could serve as a control for non-specific binding. Different concentrations of AAL were flowed over the sensor using the microfluidics, and the device spectrum was measured every 10 s. The introduction of each solution, as shown in Fig. 4a, results in a red shift in the resonance wavelengths of the two glycan-coated microrings. The difference in the shifts of the two microrings can be attributed to the difference in the surface coverage of glycans and sensitivities of the two microrings. The response of the middle microring sensor (lacking any glycan receptors but having a PEG coating) slowly shifts toward shorter wavelengths. This shift can be due to non-covalently bound linker molecules that gradually leave the surface when the analyte flows in the channel. The glycan/lectin dose–response curve is generally expected to follow a Sigmoid curve:

$$R = R_s \frac{C}{C + K_D}, \tag{6}$$

where R is the resonance shift corresponding to the concentration C; R_s is the resonance shift for the saturated surface (i.e., all binding sites occupied); and K_D is the dissociation constant for the glycan/lectin pair. Using the data for five highest concentrations, the average dissociation constant is calculated to be $K_D = 6 \pm 2$ μg/ml. After the completion of the test, the chip was dyed with the Alexa-Streptavidin dying protocol described in Section 2.3. The inset of Fig. 4a shows a fluorescence microscope image of the dyed chip, which shows the binding of Streptavidin molecules only to the microrings with immobilized glycan/lectin molecules. The turn-around-time of the sensor, defined as the saturation time of the glycan/lectin binding reaction, ranges from about 20 min for the lowest concentration (see Fig. 4a) to about a minute for the highest concentration used.

Similarly, we tested the biosensor with α2,6-disialylated biantennary N-glycan (2,6-NA2) as the bio-receptor, for detecting biotinylated Sambucus Nigra Lectin (SNA). Fig. 4b shows the corresponding resonance shifts. By fitting a Sigmoid curve to the resonance shifts for three highest concentrations, the dissociation constant is $K_D = 27 \pm 15$ μg/ml.

4.3. Multiplexed lectin detection

For the multiplexed detection experiment, we used three uncovered microrings; coating the first microring with 3FL and the last microring with 2,6-NA2 glycans. The middle microring had only PEG coating and we used its resonance shift as the reference to exclude the non-specific binding contribution.

Each glycan is specific to its respective lectin, with negligible non-specific binding to the other lectin (Smith et al., 2010; Song et al., 2011). Thus, we processed the data from each resonator independently. Two mixtures of lectins were prepared: a low concentration solution consisting of 5.4 μg/ml AAL and 10.7 μg/ml SNA, and a high concentration solution consisting of 42.8 μg/ml AAL and 85.6 μg/ml SNA. We flowed the low concentration solution for about 15 min to the sensor followed by the high concentration solution for the same period of time. The sensor response is shown in Fig. 5.

We use the data from the high concentration solution for the calibration purpose to calculate the saturated resonance shift (R_s) in Eq. (6). This calibration is necessary since the efficiency of the immobilization of the glycans changes from one round of surface chemistry to the next, which alters the number of glycan binding sites. Subsequently, the concentrations in the low concentration cycle (C_L) can be estimated by rearranging Eq. (6) to

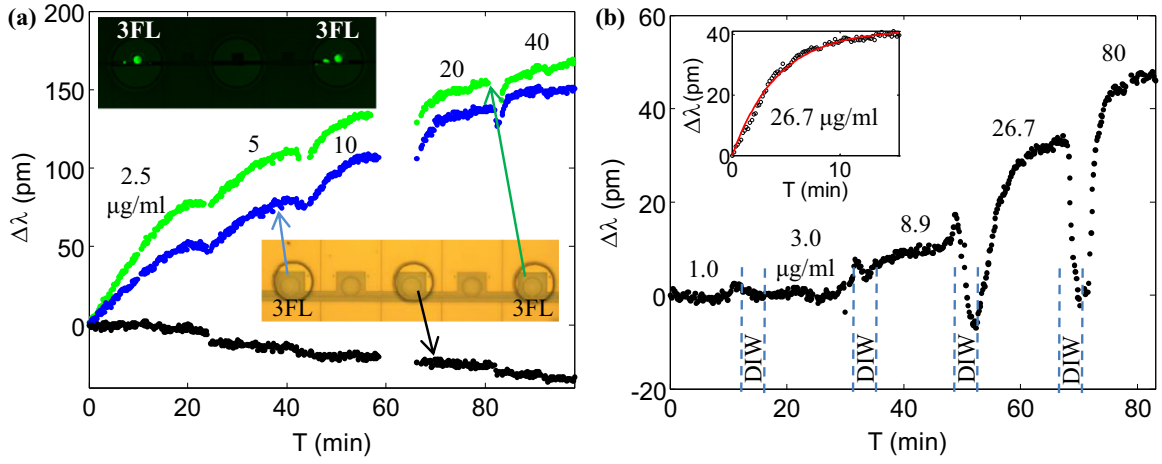

Fig. 4. The individual detection of AAL and SNA. Two separate sensor chips were prepared with their first and last microrings coated with the corresponding glycans, and the middle resonator had a PEG coating without any glycans. The concentration of the lectin in each test cycle is noted on the graph in μg/ml. The resonance shifts of the three sensing resonators are referenced to the average of the resonance shifts of the two oxide-covered resonators. (a) The binding of AAL to 3FL on the surface of the microrings. The inset shows a fluorescence microscope image of the dyed chip. (b) The average of resonance shifts of the two 2,6-NA2 coated resonators referenced to the resonance shift of the PEG-coated (middle) resonator. The inset shows the test cycle corresponding to an SNA concentration of 26.7 μg/ml.

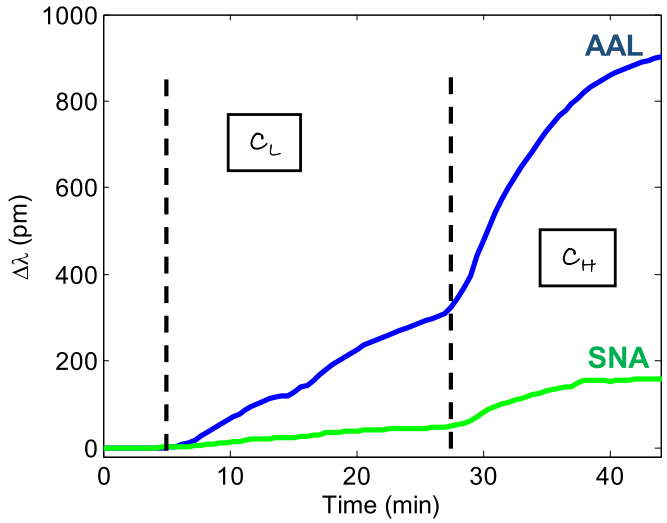

Fig. 5. Sensor response to the mixture of the two lectins (AAL and SNA). The low concentration solution is flowed to the sensor in the C_L phase, followed by the high concentration solution in the C_H phase. The resonance shift and saturation time constant for each microring depends on the concentration of the corresponding lectin and the binding dynamics of the glycan/lectin pair.

Table 1
Resonance shifts and calculated lectin concentrations from the multiplexed test.

Lectin	R_H (pm)	R_s (pm)	R_L (pm)	C_L (μg/ml)
AAL	968	1104	385	3.2
SNA	167	219	79	16

$$C_L = K_D \frac{R_L}{R_s - R_L}, \tag{7}$$

where R_L is the steady-state resonance shift for the low-concentration cycle, calculated using an exponential fit to the data. We denote the similar parameter for the high-concentration cycle by R_H. The resonance shifts and calculations are presented in Table 1.

5. Discussions

5.1. Limit of detection

With a repeatability of $3\sigma \sim 0.1$ pm for the resonance detection in our system (Ghasemi et al., 2014), and a sensitivity of 49 nm/RIU from Section 4.1, the sensor LOD is 2×10^{-6} RIU for bulk refractive index sensing. The sensitivity of the microring resonance wavelength to the deposition of an organic monolayer with a refractive index of 1.45 in water is about 109 pm/nm (resonance shift per homogeneous layer thickness, from COMSOL simulations). This leads to a minimum resolvable thickness of 1 pm that corresponds to an LOD of 1 pg/mm^2, which is in the same range as comparable integrated photonic sensor systems based on Si microrings (Luchansky et al., 2010), folded cavities (Xu et al., 2008), and liquid core optical ring resonators (LCORR) (Zhu et al., 2007).

For the detection of lectins, the sensor LOD depends linearly on the saturated response, and thus on the density of immobilized receptors on the surface. According to Eq. (7), the smallest concentration corresponding to a minimum resonance shift of $3\sigma_\lambda$ is

$$LOD \approx K_D \frac{3\sigma_\lambda}{R_s}, \tag{8}$$

assuming $R_s \gg 3\sigma_\lambda$. Hence, according to the saturated resonance shifts (R_s) in Table 1, the LOD is about 0.5 ng/ml (or 7 pM) for AAL detection, and about 12 ng/ml (or 86 pM) for SNA detection. The molecular weights of AAL and SNA are 72 kDa and 140 kDa, respectively. In the calculation of this LOD only the effects of optical, electrical, and thermal noises were included. The differences between the calculated C_L concentrations in Table 1 and the actual concentrations can originate from chip-to-chip variations in the surface chemistry, and the non-uniformity of flow originating from air bubbles in the flow cell. In complex samples, the operating parameters of the sensor may also depend on the presence of interfering species.

5.2. Coupling optimization: special cases

We optimized the waveguide-resonator coupling in Section 3 for the specific noise we measured in our setup. In this section, we discuss two alternative, common noise models: (1) intensity-independent noise and (2) relative-intensity noise. Fig. 3b includes the plots of the FOM for these noise models. It is worth noting that for an intensity-independent noise, a 6 dB undercoupled condition ($Q_c/Q_0 = 3$) leads to the optimal FOM. Since the noise is independent of the intensity, our optimization approach seeks the coupling condition that results in the sharpest resonance. Although at critical coupling the extinction is maximum, the loaded resonance curvature is smaller than the 6 dB undercoupled case. According to our optimization procedure, the 6 dB undercoupled condition is the ideal compromise between the extinction and the linewidth. At this coupling strength, the FOM is 40% smaller than that for the critically coupled case, which results in 40% improvement in the LOD (at a fixed optical power), or 40% less power consumption (for a fixed LOD).

For a relative-intensity noise, on the other hand, the optimal condition is critical coupling. In this case, the noise vanishes around the resonance wavelength of a critically coupled resonator. That is because the output light intensity vanishes at the resonance, and so does the relative-intensity noise by its definition. Hence, the critical coupling regime results in a nearly zero noise level around the resonance and it is thus the optimal design. In practice, however, an ideal relative-intensity noise that totally vanishes at the zero signal level is rare. Multiple sources of amplitude noise contributing to the aggregate amplitude noise are independent of the light reaching the detector (for instance, detector dark noise and electronic noise), and they result in residual noise.

5.3. Oxide deposition temperature for proper lift-off

We used low-temperature (100 °C) oxide for the deposition of the protective oxide layer. Although the deposition at higher temperatures (e.g., around 250 °C) results in a higher quality PECVD oxide, such high temperatures change the chemical characteristics of the resist, and the resist cannot be developed using regular developer solutions after oxide deposition. For this reason, we used low-temperature oxide deposited by an Oxford ICP PECVD tool. We also tried oxide deposition using a CHA Industries electron-beam evaporator. This method of deposition does not change the chemical characteristics of Shipley 1827 resist, but the deposition takes longer, requires periodic monitoring, and more variations were observed in the quality of the deposited layer from one fabrication round to the next.

5.4. Bioreceptor density on sensor surface

We used BioForce Nano eNabler tool to print 3FL glycan first, and then 2,6-NA2, as explained in Section 2.3. The printing process requires a high humidity (a relative humidity of about 80% in our

case) for the analyte to flow from the reservoir to the surface. This high humidity deactivates water-sensitive NHS functional groups. Therefore, the later the glycan solution is printed, the fewer NHS groups will be available for covalent immobilization of the glycan molecules. This process results in a relatively lower level of response for SNA compared to AAL in Fig. 5. This trend was observed in other similarly prepared sensor chips as well.

6. Conclusion

Total system cost is one of the commercialization challenges for highly multiplexed biosensors based on integrated photonic resonators. In this paper a label-free opto-fluidic sensor was presented that benefits from a low-cost silicon nitride device layer and silicon photodetectors. Conventional design rules of thumb recommend maximum light–matter interaction, which occurs at critical coupling for traveling-wave resonators. However, we showed that while the critical coupling condition is optimum in the presence of a relative-intensity noise, the optimum design in the presence of an ideal intensity-independent noise is an undercoupled resonator with a 6-dB extinction. The latter design has a 40% power (or equivalently, LOD) advantage over conventional critically coupled designs. For the specific noise characteristics measured in our setup, the optimal design consumes about 31% less power than a critically coupled configuration for a fixed LOD. Multiplexed label-free detection experiment was performed for Aleuria Aurantia Lectin (AAL) and Sambucus Nigra Lectin (SNA). 3FL and 2,6-NA2 glycans were used as specific bio-receptors for the detection of these lectins. Further analysis shows that the sensor limit of detection is $\sim 2 \times 10^{-6}$ RIU for bulk refractive index, ~ 1 pg/mm^2 for surface-adsorbed mass, and ~ 10 pM for the glycan/lectin pairs studied here. The performance of our sensor is comparable to the state of the art, however with the critical advantages of lower power consumption, relative structural simplicity, and low cost. The experimental and theoretical study in this paper paves the way toward the realization of highly multiplexed and dense micro-array sensors.

Contributions

F.G., A.A.E., and A.A. planned the project. F.G., E.S.H., and M.C. fabricated the photonic chip; F.G., D.S.G., A.A.E., M.C., E.S.H., and M. R. developed the surface chemistry and fluidic packaging. X.S. and R.D.C. supplied the material and protocol for glycan immobilization. F.G. and M.C. characterized the sensor. F.G., A.A.E., and D.S.G. analyzed the data. Noise performance optimization was carried out by F.G. and A.A. All authors edited and commented on the manuscript.

Acknowledgment

This work was performed in part at the Georgia Tech Institute for Electronics and Nanotechnology (IEN), a member of the National Nanotechnology Infrastructure Network, which is supported by the National Science Foundation. The authors gratefully acknowledge the staff of the IEN, especially Devin Brown. The authors thank following people for helpful discussions: Hamed Shams-Mousavi on surface chemistry; Amir Hossein Atabaki and Siva Yegnanarayanan on optical characterization; Reza Abbaspour on microfluidics fabrication; Andrew Shaw on fluorescence microscopy; and Mahmoud Mahmoud and Seth Marder on surface chemistry. This work was supported by the Defense Advanced Research Projects Agency (DARPA) under Contract no. HR 0011-10-1-0075.

References

Chamanzar, M., Soltani, M., Momeni, B., Yegnanarayanan, S., Adibi, A., 2010. Hybrid photonic surface-plasmon-polariton ring resonators for sensing applications. Appl. Phys. B 101 (1–2), 263–271.
Chao, C.-Y., Fung, W., Guo, L.J., 2006. Polymer microring resonators for biochemical sensing applications. IEEE J. Sel. Top. Quantum Electron. 12 (1), 134–142.
Ciminelli, C., Dell'Olio, F., Armenise, M.N., Soares, F.M., Passenberg, W., 2013. High performance InP ring resonator for new generation monolithically integrated optical gyroscopes. Opt. Express 21 (1), 556–564.
Claes, T., Bogaerts, W., Bienstman, P., 2010. Experimental characterization of a silicon photonic biosensor consisting of two cascaded ring resonators based on the vernier-effect and introduction of a curve fitting method for an improved detection limit. Opt. Express 18 (22), 22747–22761.
De Vos, K., Bartolozzi, I., Schacht, E., Bienstman, P., Baets, R., 2007. Silicon-on-insulator microring resonator for sensitive and label-free biosensing. Opt. Express 15 (12), 7610–7615.
De Vos, K., Girones, J., Popelka, S., Schacht, E., Baets, R., Bienstman, P., 2009. SOI optical microring resonator with poly (ethylene glycol) polymer brush for label-free biosensor applications. Biosens. Bioelectron. 24 (8), 2528–2533.
Della Corte, F.G., Cocorullo, G., Iodice, M., Rendina, I., 2000. Temperature dependence of the thermo-optic coefficient of InP, GaAs, and SiC from room temperature to 600 K at the wavelength of 1.5 μm. Appl. Phys. Lett. 77 (11), 1614–1616.
Fan, X., White, I.M., Shopova, S.I., Zhu, H., Suter, J.D., Sun, Y., 2008. Sensitive optical biosensors for unlabeled targets: a review. Anal. Chim. Acta 620 (1), 8–26.
Fard, S.T., Donzella, V., Schmidt, S.A., Flueckiger, J., Grist, S.M., Talebi Fard, P., Wu, Y., Bojko, R.J., Kwok, E., Jaeger, N.A., et al., 2014. Performance of ultra-thin SOI-based resonators for sensing applications. Opt. Express 22 (12), 14166–14179.
Ghasemi, F., Chamanzar, M., Eftekhar, A.A., Adibi, A., 2014. An efficient technique for the reduction of wavelength noise in resonance-based integrated photonic sensors. Analyst 139 (22), 5902–5911.
Ghasemi, F., Eftekhar, A.A., Gottfried, D.S., Song, X., Cummings, R.D., Adibi, A., 2013. Self-referenced silicon nitride array microring biosensor for toxin detection using glycans at visible wavelength. In: SPIE BiOS. International Society for Optics and Photonics, pp. 85940A–85940A-9.
Ghasemi, F., Zhou, H., Adibi, A., 2015. Closed-form relations for resonance detection error using statistical analysis of amplitude noise. IEEE J. Sel. Top. Quantum Electron. 21 (4), 9000308, San Francisco, CA , United States.
Gülşen, G., Naci Inci, M., 2002. Thermal optical properties of TiO_2 films. Opt. Mater. 18 (4), 373–381.
Gylfason, K.B., Carlborg, C.F., Kazmierczak, A., Dortu, F., Vivien, L., Barrios, C.A., van der Wijngaart, W., Stemme, G., et al., 2010. On-chip temperature compensation in an integrated slot-waveguide ring resonator refractive index sensor array. Opt. Express 18 (4), 3226–3237.
Heideman, R., Hoekman, M., Schreuder, E., 2012. Triplex-based integrated optical ring resonators for lab-on-a-chip and environmental detection. IEEE J. Sel. Top. Quantum Electron. 18 (5), 1583–1596.
Hunt, H.K., Armani, A.M., 2010. Label-free biological and chemical sensors. Nanoscale 2 (9), 1544–1559.
Kirk, J.T., Fridley, G.E., Chamberlain, J.W., Christensen, E.D., Hochberg, M., Ratner, D. M., 2011. Multiplexed inkjet functionalization of silicon photonic biosensors. Lab Chip 11 (7), 1372–1377.
Lee, S., Eom, S.C., Chang, J.S., Huh, C., Sung, G.Y., Shin, J.H., 2010. Label-free optical biosensing using a horizontal air-slot SiN_x microdisk resonator. Opt. Express 18 (20), 20638–20644.
Luchansky, M.S., Washburn, A.L., Martin, T.A., Iqbal, M., Gunn, L.C., Bailey, R.C., 2010. Characterization of the evanescent field profile and bound mass sensitivity of a label-free silicon photonic microring resonator biosensing platform. Biosens. Bioelectron. 26 (4), 1283–1291.
Park, M.K., Kee, J.S., Quah, J.Y., Netto, V., Song, J., Fang, Q., La Fosse, E.M., Lo, G.-Q., 2013. Label-free aptamer sensor based on silicon microring resonators. Sens. Actuators B: Chem. 176, 552–559.
Qavi, A.J., Bailey, R.C., 2010. Multiplexed detection and label-free quantitation of microRNAs using arrays of silicon photonic microring resonators. Angew. Chem. 122 (27), 4712–4715.
Quan, X., Fry, E.S., 1995. Empirical equation for the index of refraction of seawater. Appl. Opt. 34 (18), 3477–3480.
Rong, G., Ryckman, J.D., Mernaugh, R.L., Weiss, S.M., 2008. Label-free porous silicon membrane waveguide for DNA sensing. Appl. Phys. Lett. 93 (16), 161109.
Shah Hosseini, E., Yegnanarayanan, S., Atabaki, A.H., Soltani, M., Adibi, A., 2010. Systematic design and fabrication of high-q single-mode pulley-coupled planar silicon nitride microdisk resonators at visible wavelengths. Opt. Express 18 (3), 2127–2136.
Smith, D.F., Song, X., Cummings, R.D., 2010. Chapter nineteen-use of glycan microarrays to explore specificity of glycan-binding proteins. Methods Enzymol. 480, 417–444.
Soltani, M., Yegnanarayanan, S., Li, Q., Adibi, A., 2010. Systematic engineering of waveguide-resonator coupling for silicon microring/microdisk/racetrack resonators: theory and experiment. IEEE J. Quantum Electron. 46 (8), 1158–1169.

Song, X., Lasanajak, Y., Xia, B., Heimburg-Molinaro, J., Rhea, J.M., Ju, H., Zhao, C., Molinaro, R.J., Cummings, R.D., Smith, D.F., 2011. Shotgun glycomics: a microarray strategy for functional glycomics. Nat. Methods 8 (1), 85–90.
Song, X., Xia, B., Stowell, S.R., Lasanajak, Y., Smith, D.F., Cummings, R.D., 2009. Novel fluorescent glycan microarray strategy reveals ligands for galectins. Chem. Biol. 16 (1), 36–47.
von Gunten, S., Smith, D.F., Cummings, R.D., Riedel, S., Miescher, S., Schaub, A., Hamilton, R.G., Bochner, B.S., 2009. Intravenous immunoglobulin contains a broad repertoire of anticarbohydrate antibodies that is not restricted to the IgG2 subclass. J. Allergy Clin. Immunol. 123 (June (6)), 1268–1276, e15.
Washburn, A.L., Luchansky, M.S., Bowman, A.L., Bailey, R.C., 2009. Quantitative, label-free detection of five protein biomarkers using multiplexed arrays of silicon photonic microring resonators. Anal. Chem. 82 (1), 69–72.
White, I.M., Fan, X., 2008. On the performance quantification of resonant refractive index sensors. Opt. Express 16 (2), 1020–1028.
Xu, D., Densmore, A., Delâge, A., Waldron, P., McKinnon, R., Janz, S., Lapointe, J., Lopinski, G., Mischki, T., Post, E., et al., 2008. Folded cavity SOI microring sensors for high sensitivity and real time measurement of biomolecular binding. Opt. Express 16 (19), 15137–15148.
Zhu, H., White, I.M., Suter, J.D., Dale, P.S., Fan, X., 2007. Analysis of biomolecule detection with optofluidic ring resonator sensors. Opt. Express 15 (15), 9139–9146.